Research Article | Vol. 26, No. 7 | 2 Apr 2018 | OPTICS EXPRESS 8866
Optics EXPRESS

Nonlinear dynamic of picosecond pulse propagation in atmospheric air-filled hollow core fibers

SEYEDMOHAMMAD ABOKHAMIS MOUSAVI,* HANS CHRISTIAN HANSEN MULVAD, NATALIE V. WHEELER, PETER HORAK, JOHN HAYES, YONG CHEN, THOMAS D. BRADLEY, SHAIF-UL ALAM, SEYED REZA SANDOGHCHI, ERIC NUMKAM FOKOUA, DAVID J. RICHARDSON, AND FRANCESCO POLETTI

Optoelectronics Research Centre, University of Southampton, Southampton SO17 1BJ, UK
*sam1e12@soton.ac.uk

Abstract: Atmospheric air-filled hollow core (HC) fibers, representing the simplest yet reliable form of gas-filled hollow core fiber, show remarkable nonlinear properties and have several interesting applications such as pulse compression, frequency conversion and supercontinuum generation. Although the propagation of sub-picosecond and few hundred picosecond pulses are well-studied in air-filled fibers, the nonlinear response of air to pulses with a duration of a few picoseconds has interesting features that have not yet been explored fully. Here, we experimentally and theoretically study the nonlinear propagation of ~6 ps pulses in three different types of atmospheric air-filled HC fiber. With this pulse length, we were able to explore different nonlinear characteristics of air at different power levels. Using in-house-fabricated, state-of-the-art HC photonic bandgap, HC tubular and HC Kagomé fibers, we were able to associate the origin of the initial pulse broadening process in these fibers to rotational Raman scattering (RRS) at low power levels. Due to the broadband and low loss transmission window of the HC Kagomé fiber we used, we observed the transition from initial pulse broadening (by RRS) at lower powers, through long-range frequency conversion (2330 cm^{-1}) with the help of vibrational Raman scattering, to broadband (~700 nm) supercontinuum generation at high power levels. To model such a wide range of nonlinear processes in a unified approach, we have implemented a semi-quantum model for air into the generalized nonlinear Schrodinger equation, which surpasses the limits of the common single damping oscillator model in this pulse length regime. The model has been validated by comparison with experimental results and provides a powerful tool for the design, modeling and optimization of nonlinear processes in air-filled HC fibers.

OCIS codes: (060.4005) Microstructured fibers; (190.5650) Raman effect; (060.4370) Nonlinear optics, fibers; (320.6629) Supercontinuum generation; (060.7140) Ultrafast processes in fibers.

References and links

1. C. L. Hoy, O. Ferhanoğlu, M. Yildirim, W. Piyawattanametha, H. Ra, O. Solgaard, and A. Ben-Yakar, "Optical design and imaging performance testing of a 9.6-mm diameter femtosecond laser microsurgery probe," Opt. Express **19**(11), 10536–10552 (2011).
2. B. N. Chichkov, C. Momma, S. Nolte, F. von Alvensleben, and A. Tünnermann, "Femtosecond, picosecond and nanosecond laser ablation of solids," Appl. Phys., A Mater. Sci. Process. **63**(2), 109–115 (1996).
3. M. Gu, D. Bird, D. Day, L. Fu, and D. Morrish, *Femtosecond Biophotonics: Core Technology and Applications* (Cambridge University Press, 2010).
4. A. V. Smith and B. T. Do, "Bulk and surface laser damage of silica by picosecond and nanosecond pulses at 1064 nm," Appl. Opt. **47**(26), 4812–4832 (2008).
5. F. Poletti, N. Petrovich Marco, and J. Richardson David, "Hollow-core photonic bandgap fibers: technology and applications," Nanophotonics **2**(5-6), 315 (2013).
6. Y. Chen, Z. Liu, S. R. Sandoghchi, G. T. Jasion, T. D. Bradley, E. Numkam Fokoua, J. R. Hayes, N. V. Wheeler, D. R. Gray, B. J. Mangan, R. Slavik, F. Poletti, M. N. Petrovich, and D. J. Richardson, "Multi-kilometer Long,

#320621 https://doi.org/10.1364/OE.26.008866
Journal © 2018 Received 26 Jan 2018; accepted 28 Feb 2018; published 27 Mar 2018

Optics EXPRESS

Longitudinally Uniform Hollow Core Photonic Bandgap Fibers for Broadband Low Latency Data Transmission," J. Lightwave Technol. **34**(1), 104–113 (2016).
7. P. S. J. Russell, P. Hölzer, W. Chang, A. Abdolvand, and J. C. Travers, "Hollow-core photonic crystal fibres for gas-based nonlinear optics," Nat. Photonics **8**(4), 278–286 (2014).
8. Y. Y. Wang, N. V. Wheeler, F. Couny, P. J. Roberts, and F. Benabid, "Low loss broadband transmission in hypocycloid-core Kagome hollow-core photonic crystal fiber," Opt. Lett. **36**(5), 669–671 (2011).
9. Y. Wang, F. Couny, P. J. Roberts, and F. Benabid, "Low loss broadband transmission in optimized core-shape kagome hollow-core PCF," in *Conference on Lasers and Electro-Optics 2010*, OSA Technical Digest (CD) (Optical Society of America, 2010), CPDB4.
10. L. Vincetti and V. Setti, "Waveguiding mechanism in tube lattice fibers," Opt. Express **18**(22), 23133–23146 (2010).
11. F. Poletti, "Nested antiresonant nodeless hollow core fiber," Opt. Express **22**(20), 23807–23828 (2014).
12. J. Hayes, S. Sandoghchi, T. Bradley, Z. Liu, R. Slavík, M. A. Gouveia, N. Wheeler, G. Jasion, Y. Chen, E. Numkam-Fokoua, M. Petrovich, D. Richardson, and F. Poletti, "Antiresonant hollow core fiber with octave spanning bandwidth for short haul data communications," in *Optical Fiber Communication Conference Postdeadline Papers,* (Optical Society of America, 2016), p. Th5A.3.
13. E. T. J. Nibbering, G. Grillon, M. A. Franco, B. S. Prade, and A. Mysyrowicz, "Determination of the inertial contribution to the nonlinear refractive index of air, N2, and O2 by use of unfocused high-intensity femtosecond laser pulses," J. Opt. Soc. Am. B **14**(3), 650–660 (1997).
14. M. Mlejnek, E. M. Wright, and J. V. Moloney, "Dynamic spatial replenishment of femtosecond pulses propagating in air," Opt. Lett. **23**(5), 382–384 (1998).
15. Q. Lin and G. P. Agrawal, "Raman response function for silica fibers," Opt. Lett. **31**(21), 3086–3088 (2006).
16. F. Guichard, A. Giree, Y. Zaouter, M. Hanna, G. Machinet, B. Debord, F. Gérôme, P. Dupriez, F. Druon, C. Hönninger, E. Mottay, F. Benabid, and P. Georges, "Nonlinear compression of high energy fiber amplifier pulses in air-filled hypocycloid-core Kagome fiber," Opt. Express **23**(6), 7416–7423 (2015).
17. K. F. Mak, J. C. Travers, N. Y. Joly, A. Abdolvand, and P. S. Russell, "Two techniques for temporal pulse compression in gas-filled hollow-core kagomé photonic crystal fiber," Opt. Lett. **38**(18), 3592–3595 (2013).
18. A. R. Bhagwat and A. L. Gaeta, "Nonlinear optics in hollow-core photonic bandgap fibers," Opt. Express **16**(7), 5035–5047 (2008).
19. Y. P. Yatsenko, E. N. Pleteneva, A. G. Okhrimchuk, A. V. Gladyshev, A. F. Kosolapov, A. N. Kolyadin, and I. A. Bufetov, "Multiband supercontinuum generation in an air-core revolver fibre," Quantum Electron. **47**(6), 553–560 (2017).
20. B. Debord, F. Gérôme, C. Hoenninger, E. Mottay, A. Husakou, and F. Benabid, "Milli-Joule energy-level comb and supercontinuum generation in atmospheric air-filled inhibited coupling Kagome fiber," in *CLEO: 2015 Postdeadline Paper Digest*, (Optical Society of America, 2015), JTh5C.4.
21. B. Debord, M. Alharbi, L. Vincetti, A. Husakou, C. Fourcade-Dutin, C. Hoenninger, E. Mottay, F. Gérôme, and F. Benabid, "Multi-meter fiber-delivery and pulse self-compression of milli-Joule femtosecond laser and fiber-aided laser-micromachining," Opt. Express **22**(9), 10735–10746 (2014).
22. Y. P. Yatsenko, A. A. Krylov, A. D. Pryamikov, A. F. Kosolapov, A. N. Kolyadin, A. V. Gladyshev, and I. A. Bufetov, "Propagation of femtosecond pulses in a hollow-core revolver fibre," Quantum Electron. **46**(7), 617–626 (2016).
23. P. Jaworski, F. Yu, R. R. Maier, W. J. Wadsworth, J. C. Knight, J. D. Shephard, and D. P. Hand, "Picosecond and nanosecond pulse delivery through a hollow-core Negative Curvature Fiber for micro-machining applications," Opt. Express **21**(19), 22742–22753 (2013).
24. C. Li, K. P. Rishad, P. Horak, Y. Matsuura, and D. Faccio, "Spectral broadening and temporal compression of ~ 100 fs pulses in air-filled hollow core capillary fibers," Opt. Express **22**(1), 1143–1151 (2014).
25. F. Emaury, C. F. Dutin, C. J. Saraceno, M. Trant, O. H. Heckl, Y. Y. Wang, C. Schriber, F. Gerome, T. Südmeyer, F. Benabid, and U. Keller, "Beam delivery and pulse compression to sub-50 fs of a modelocked thin-disk laser in a gas-filled Kagome-type HC-PCF fiber," Opt. Express **21**(4), 4986–4994 (2013).
26. Y. Chen, H. C. Mulvad, S. Sandoghchi, E. Numkam Fokoua, T. Bradley, J. Hayes, N. Wheeler, G. Jasion, S.-U. Alam, F. Poletti, M. Petrovich, and D. J. Richardson, "First Demonstration of Low Loss, Bend Insensitive 37-Cell Hollow-Core Photonic Bandgap Fiber at 1μm for High Power Delivery Applications," in *Conference on Lasers and Electro-Optics*, OSA Technical Digest (2016) (Optical Society of America, 2016), STu4P.1.
27. N. V. Wheeler, T. D. Bradley, J. R. Hayes, M. A. Gouveia, S. Liang, Y. Chen, S. R. Sandoghchi, S. M. Abokhamis Mousavi, F. Poletti, M. N. Petrovich, and D. J. Richardson, "Low-loss Kagome hollow-core fibers operating from the near- to the mid-IR," Opt. Lett. **42**(13), 2571–2574 (2017).
28. W. Ding and Y. Wang, "Analytic model for light guidance in single-wall hollow-core anti-resonant fibers," Opt. Express **22**(22), 27242–27256 (2014).
29. A. Hartung, J. Kobelke, A. Schwuchow, K. Wondraczek, J. Bierlich, J. Popp, T. Frosch, and M. A. Schmidt, "Double antiresonant hollow core fiber--guidance in the deep ultraviolet by modified tunneling leaky modes," Opt. Express **22**(16), 19131–19140 (2014).
30. L. Chen, G. J. Pearce, T. A. Birks, and D. M. Bird, "Guidance in Kagome-like photonic crystal fibres I: analysis of an ideal fibre structure," Opt. Express **19**(7), 6945–6956 (2011).
31. B. Debord, A. Amsanpally, M. Chafer, A. Baz, M. Maurel, J. M. Blondy, E. Hugonnot, F. Scol, L. Vincetti, F. Gérôme, and F. Benabid, "Ultralow transmission loss in inhibited-coupling guiding hollow fibers," Optica **4**(2), 209 (2017).
32. F. Yu and J. C. Knight, "Negative Curvature Hollow-Core Optical Fiber," IEEE J. Sel. Top. Quantum Electron. **22**(2), 146–155 (2016).

Optics EXPRESS

33. B. Debord, M. Alharbi, T. Bradley, C. Fourcade-Dutin, Y. Y. Wang, L. Vincetti, F. Gérôme, and F. Benabid, "Hypocycloid-shaped hollow-core photonic crystal fiber Part I: arc curvature effect on confinement loss," Opt. Express **21**(23), 28597–28608 (2013).
34. F. Poletti, M. N. Petrovich, and D. J. Richardson, "Hollow-core photonic bandgap fibers: technology and applications," Nanophotonics **2**(5-6), 4 (2013).
35. M. A. Finger, N. Y. Joly, T. Weiss, and P. S. Russell, "Accuracy of the capillary approximation for gas-filled kagomé-style photonic crystal fibers," Opt. Lett. **39**(4), 821–824 (2014).
36. A. Börzsönyi, Z. Heiner, M. P. Kalashnikov, A. P. Kovács, and K. Osvay, "Dispersion measurement of inert gases and gas mixtures at 800 nm," Appl. Opt. **47**(27), 4856–4863 (2008).
37. S. A. Mousavi, S. R. Sandoghchi, D. J. Richardson, and F. Poletti, "Broadband high birefringence and polarizing hollow core antiresonant fibers," Opt. Express **24**(20), 22943–22958 (2016).
38. J. R. Hayes, S. R. Sandoghchi, T. D. Bradley, Z. Liu, R. Slavik, M. A. Gouveia, N. V. Wheeler, G. Jasion, Y. Chen, E. N. Fokoua, M. N. Petrovich, D. J. Richardson, and F. Poletti, "Antiresonant Hollow Core Fiber With an Octave Spanning Bandwidth for Short Haul Data Communications," J. Lightwave Technol. **35**(3), 437–442 (2017).
39. "TruMicro Series 5000", retrieved *http://www.uk.trumpf.com/en/products/laser-technology/products/solid-state-lasers/short-pulsed-lasers/trumicro-series-5000.html*.
40. G. P. Agrawal, *Nonlinear Fiber Optics* (Academic Press, 2007).
41. Y. R. Shen and N. Bloembergen, "Theory of Stimulated Brillouin and Raman Scattering," Phys. Rev. **137**(6A), A1787–A1805 (1965).
42. A. V. Gorbach and D. V. Skryabin, "Soliton self-frequency shift, non-solitonic radiation and self-induced transparency in air-core fibers," Opt. Express **16**(7), 4858–4865 (2008).
43. J. Lægsgaard and P. J. Roberts, "Modeling of High-Power Pulse Compression and Soliton Formation in Hollow-Core Photonic Bandgap Fibers," in Advances in Optical Sciences Congress, OSA Technical Digest (CD) (Optical Society of America, 2009), paper IMG1.
44. K. J. Blow and D. Wood, "Theoretical description of transient stimulated Raman scattering in optical fibers," IEEE J. Quantum Electron. **25**(12), 2665–2673 (1989).
45. J. M. Brown and A. Carrington, *Rotational Spectroscopy of Diatomic Molecules* (Cambridge University Press, 2003).
46. A. P. Hickman, J. A. Paisner, and W. K. Bischel, "Theory of multiwave propagation and frequency conversion in a Raman medium," Phys. Rev. A Gen. Phys. **33**(3), 1788–1797 (1986).
47. J. R. Peñano, P. Sprangle, P. Serafim, B. Hafizi, and A. Ting, "Stimulated Raman scattering of intense laser pulses in air," Phys. Rev. E Stat. Nonlin. Soft Matter Phys. **68**(5), 056502 (2003).
48. W. D. Brewer, H. Haken, and H. C. Wolf, *Molecular Physics and Elements of Quantum Chemistry: Introduction to Experiments and Theory* (Springer Berlin Heidelberg, 2013).
49. L. Martinsson, P. E. Bengtsson, M. Aldén, S. Kröll, and J. Bonamy, "A test of different rotational Raman linewidth models: Accuracy of rotational coherent anti-Stokes Raman scattering thermometry in nitrogen from 295 to 1850 K," J. Chem. Phys. **99**(4), 2466–2477 (1993).
50. A. M. Zheltikov, "Raman response function of atmospheric air," Opt. Lett. **32**(14), 2052–2054 (2007).
51. L. A. Rahn and R. E. Palmer, "Studies of nitrogen self-broadening at high temperature with inverse Raman spectroscopy," J. Opt. Soc. Am. B **3**(9), 1164 (1986).
52. M. E. Kooi, L. Ulivi, and J. A. Schouten, "Vibrational Spectra of Nitrogen in Simple Mixtures at High Pressures," Int. J. Thermophys. **20**(3), 867–876 (1999).
53. G. Agrawal, *Nonlinear Fiber Optics* (Academic Press, October 2012), p. 648.
54. X. Liu, "Adaptive higher-order split-step Fourier algorithm for simulating lightwave propagation in optical fiber," Opt. Commun. **282**(7), 1435–1439 (2009).

1. Introduction

Recent demonstrations of Gigawatt class pulsed power lasers with high repetition rates in commercial tabletop form have introduced new developments in some applications such as micro-surgery [1], micro-machining [2], and biophotonics [3]. However, as conventional solid-core fibers can only handle pulse powers less than MW at picosecond range [4], due to their low damage threshold and high nonlinearity, the delivery of such ultra-high power pulses in a flexible and reliable form is mostly limited to free space setups. Hollow core fibers (HCFs), can offer much higher power delivery capability with considerably higher damage threshold and significantly lower nonlinearity [5]. Among the different types of HCFs, hollow core photonic bandgap fibers (HC-PBGFs) have demonstrated the lowest loss and the fabrication technology is relatively mature [6]. However, they suffer a lower damage threshold in comparison to other forms of HCF due to the larger overlap between the guided optical field and cladding glass [7]. On the other hand, recently introduced and rapidly developing HCFs with a negative-curvature core boundary (hypocycloid) (e.g. HC Kagomé fiber (HC-KF) and HC Tubular fiber (HC-TFs)) [8–12] offer a considerably lower overlap between the air-guided field and cladding glass, leading to a significant increase in damage

Optics EXPRESS

threshold, to levels well beyond that of HC-PBGFs. Furthermore, at wavelengths around 1 μm and below, HC-KFs and HC-TFs can now achieve a loss comparable to, or even lower than, HC-PBGFs. These features, alongside their multiple and broad transmission windows, make them attractive to study and exploit broadband nonlinear processes in gases, such as stimulated Raman scattering (SRS), frequency comb generation, and supercontinuum generation (SG) [7].

The ambient air that can be found in the core of HCFs, has an almost two orders of magnitude lower nonlinearity (~6×10^{-23} m^2/W) than silica glass (2×10^{-22} m^2/W) [13–15]. However, its nonlinearity can still have significant effects on the propagation of high peak power pulses, that can lead to spectral broadening, pulse distortion and ultimately loss of power, all of which are typically detrimental in power delivery applications. For some applications, however, the nonlinear processes can be exploited for pulse modification [16, 17], new frequency generation [18], or even broad SG with a very high power density due to the very high damage threshold of HCFs and the confined gas within the core [7, 19]. The simplicity of air-filled HCFs, combined with their very long light-matter interactions, motivated the exploration of potential applications in recent works [20, 21]. To support such experimental works there is a clear need for appropriate tools for modeling the pulse propagation in air-filled fibers.

In recent years, there have been several experimental studies on pulse propagation in air-filled HCFs in different pulse regimes, ranging from few femtosecond to nanosecond pulses [20, 22–25]. Each experiment has shown a specific characteristic of the nonlinear processes in air. Yet, to the best of our knowledge, a study that illustrates a broad range of nonlinear phenomena and observes clear fingerprints of both vibrational Raman scattering (VRS) and rotational Raman scattering (RRS) has not yet been reported. The ultra-short pulse regime (sub-ps duration) can introduce a broad supercontinuum expanding through many fiber transmission bands, as demonstrated in different types of HCFs including HC-KFs and HC-TFs [19, 20]. Although, in this regime, very interesting results are obtained through a variety of nonlinear processes, the clear signature of Raman scattering is absent. In this case, the mixed effect of four wave mixing (FWM) and SRS in the output pulse, and more specifically the lack of a clear sign of VRS, significantly reduce the ability to study in detail the RRS and VRS processes. Furthermore, it is challenging to resolve the evolution from an initial single dominant Raman/FWM excitation to a broad supercontinuum spectrum.

In contrast, long pulses (e.g. hundreds of picosecond to nanosecond pulses) show much more detail in terms of Raman scattering and can produce sharp and clear Raman peaks even at very high powers [20]. In this regime, not only can VRS be observed distinctively, but the RRS peaks corresponding to higher order Stokes can be distinguished, in contrast to the broadening effects seen with femtosecond pulses. However, to achieve broad SG in this regime, impractically high power input pulses are necessary, which limits the understanding of the broadening process and practicality of the system. Recently, the dynamics of pulse propagation in both regimes has been experimentally demonstrated in two separate atmospheric air-filled HCFs (negative-curvature HC-KFs) pumped by 100 fs and 300 ps pulses in different setups [20]. Here we study the nonlinear evolution dynamics for pulse durations in the middle of the aforementioned range, which complements existing results and helps constructing a comprehensive picture of the nonlinear response in air-filled HCFs.

In this work, by selecting appropriate pulse parameters we experimentally observed a variety of nonlinear processes. In addition to variations in the pulse characteristics (e.g. pulse length and peak power), we have experimentally compared different types of HCFs (i.e. HC-PBGF, HC-KF and HC-TF), in order to provide insight into the influence of the HCF itself. Furthermore, in order to be able to theoretically reproduce the results over a broad spectral range, we have implemented a semi-quantum model of the roto-vibrational Raman process in bi-atomic molecules to simulate the nonlinear behavior of air with a sufficiently good precision. Using this model, the nonlinear dynamics of pulse propagation have been simulated in different scenarios yielding a very good agreement with experimental results. This provides a useful tool for analyzing the nonlinear behavior of air-filled HCFs.

Optics EXPRESS

2. Experimental setup and results

2.1 Fiber characteristics

In addition to their ability to confine gas, guide light for a long distance and therefore provide long gas-light interaction lengths, HCFs can profoundly influence the pulse propagation dynamics. Thus, their optical and geometrical characteristics are of critical importance in determining the pulse propagation dynamics, as exemplified in this study.

Based on their guidance mechanism, HCFs can be categorized into two major types: photonic bandgap fibers (PBGFs) and anti-resonance/inhibited coupling fibers (ARFs). In this work, to study the effect of the fiber characteristics on the nonlinear behavior of air, we have experimentally explored pulse propagation in three different designs of in-house-fabricated HCFs, more specifically: HC-PBGF [26], HC negative-curvature Kagomé (HC-KF) [27] and HC nodeless tubular (HC-TF) fibers. All the fibers used in this study represent, or are similar to, the state-of-the-art in their respective categories. While the guidance mechanism is clear in the first type (HC-PBGF), in the last two cases the guidance mechanism has been associated either to anti-resonance effects from glass membranes adjacent to air-core [28–30], or to inhibited coupling effect between core mode and cladding modes [31–33]. Here, without any intention to dive into any explanation of their guidance mechanism, the fibers have been chosen for their great potential to generate gas-based nonlinear processes and for the sake of studying the effects, challenges, and performance of our model.

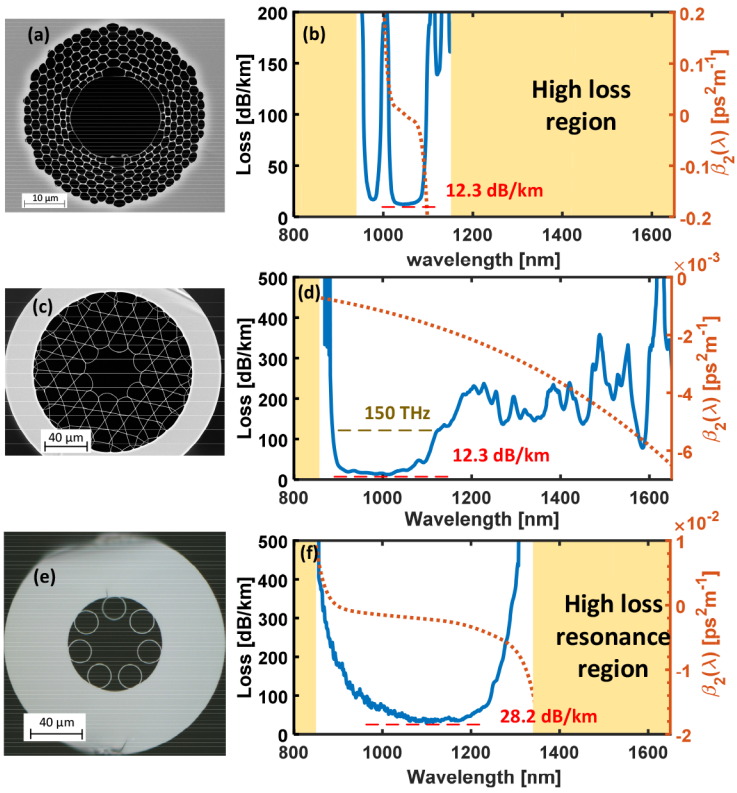

Fig. 1. Scanning electron micrographs (SEMs) of the cross-section of fabricated (a) HC-PBGF, (c) HC-KF, (e) the optical microscopic image of the cross-section of fabricated HC-TF. The loss and dispersion profile of (b) HC-PBGF, (d) HC-KF, (f) HC-TF.

HC-PBGFs, despite their narrow transmission window, have shown the lowest experimental loss among any other type of HCFs [34]. Here, we have fabricated and used a 37-cell HC-PBGF to achieve very low loss; the fiber cross section is shown in the scanning

Optics EXPRESS

electron micrograph (SEM) image in Fig. 1(a). The fiber has a core diameter of ~21.5μm and a main low loss transmission window from 1010 nm to 1096 nm. Its average loss is 13.6 dB/km and the lowest loss is 12.3 dB/km at 1046 nm (one of the best values ever reported for this kind of fiber). The measured cutback loss and calculated dispersion profile (found using commercial finite element (FEM) mode solver (COMSOL)) are shown in Fig. 1(b). Although the HC-PBGFs have a very low experimental loss, the significant overlap between the air-guided field and the cladding glass and their narrow transmission window limit their usage for high power applications and broadband nonlinear processes.

On the other hand, HC-KFs with higher damage threshold and broad multiband transmission windows can overcome the limitations of HC-PBGFs. Here, we use an in-house-fabricated 7-cell HC-KF with low loss and low bend loss (in comparison to other ARFs) [27]. The fiber has a large bandwidth centered around a wavelength of 1 μm, which is perfectly matched to our ps source. Figure 1(c) shows an SEM image of the cross-section of the fiber, which has a core diameter of 43 μm and an average core wall thickness of ~375 nm. The minimum loss of 12.3 dB/km is at 1010 nm and the 3 dB bandwidth is 150 nm. Its transmission window spans from 850 nm to 1700 nm, with an average loss of less than 200 dB/km as shown in Fig. 1(d). This broad transmission window makes the fiber a suitable host for the observation of wideband nonlinear processes. To simulate its dispersion, we have used a well-developed, suitably modified model based on the analytical dispersion of a hollow capillary, which was proven to be accurate enough for the spectral range of this work [35]:

$$\beta(\omega) = \frac{\omega}{c}\sqrt{n_{gas}^2(\omega,P,T) - \left(\frac{2.4048c}{\omega \cdot a(\omega)}\right)^2} \qquad (1)$$

Here c is the speed of light, $a(\omega) = a_{AP}/(1+0.065(2\pi c)^2/(\omega^2 a_{AP} t))$ where a_{AP} is an area-preserving core diameter of the HC-KF and t is the thickness of the core-surrounding glass membranes [35]. $n_{gas}(\omega,P,T)$ is the refractive index of the gas inside the fiber core and is a function of pressure (P) and temperature (T). Using Eq. (1) and a known model for air [36], we calculated the dispersion of our HC-KF at experimental conditions ($T \approx 290$ K°, $P \approx 1$ *atm*) as presented in Fig. 1(d). According to our simulations, the percentage of air-guided field in the cladding glass for this fiber is of the order of 10^{-5}, which leads to a high damage threshold (approximately two orders of magnitude higher than that of HC-PBGF [7]). Although this fiber has a higher order transmission window below 800 nm in addition to the fundamental one that would make it possible to explore inter-transmission band nonlinear processes, this work only focuses on the study and observation of nonlinearity in the fundamental transmission window.

Another type of HC negative-curvature fiber, with a reasonably low loss and ultra-broad multiband transmission windows, is HC-TF. Recent studies have shown the potential of these fibers to ultimately achieve a lower level of loss and greater polarization control than HC-PBGFs [11, 31, 37] and an octave-spanning version has been demonstrated recently with loss compatible with short range data transmission applications [38]. Here, we use an in-house-made 7-tube silica HC-TF with a core diameter of ~35.8 μm and an inner jacket tube diameter of ~76.7 μm. Figure 1(e) shows an optical microscopic image of the fiber cross-section. With an average tube thickness of ~775 nm, the second low loss antiresonance band of the fiber is located between 850 and 1355 nm. The fibre loss in this transmission window is shown in Fig. 1(f) alongside its simulated dispersion profile using the FEM mode solver similar to [38].

2.2 Experimental setup

We have used a commercially available Trumpf TruMicro 5050© [39] laser for our experiments. This source produces ~6 ps pulses with a 200kHz repetition rate at 1030 nm and variable energy of up to 250 μJ per pulse (average power ≈50W). The output is a collimated beam of diameter 5.4 mm, and the M^2 value is 1.08. To couple the laser pulses into the fiber,

Optics EXPRESS

we used a coupling system composed of a variable beam expander (Jenoptik 1x-4x, AE 1614, 1030-1080 nm, transmission ≥97%) followed by a focusing lens (Thorlabs LA4148-B-ML, fused silica plan-convex lens with 50mm focal length, BBAR coating 650-1050nm), Fig. 2.

To maximize the power launched into the fundamental mode of the fiber, the fiber input facet is positioned using a micrometer positioning stage at the focal point of the focusing lens. The beam expander is used to adjust the width of the collimated beam (here operated in reverse to reduce the beam diameter), such that a beam waist with the optimum width for a fundamental mode launch of each fiber is obtained at the position of the fiber input. The beam expander is fine-tuned by monitoring and maximizing the output power of the fiber (measured using a Gentec UP55N-300F-H9-D0 power meter) which indicates an optimum fundamental mode launch due to the substantially higher propagation losses of higher-order modes. As an additional precaution, a camera is used to monitor and detect scattered light from the fiber input facet. The amount of scattered light from the glass microstructure is minimized by fine-tuning the fiber input position, which further reduces the risk of damage to the input facet. The fiber under test is loosely coiled to approximately 30-40cm coil diameter. The output power of the fiber is measured using a power meter (Gentec UP55N-300F-H9-D0). To measure the optical spectrum, a small portion of the output beam is reflected off a glass wedge and coupled into an optical spectrum analyzer (OSA, Ando AQ6317B, 600-1750 nm).

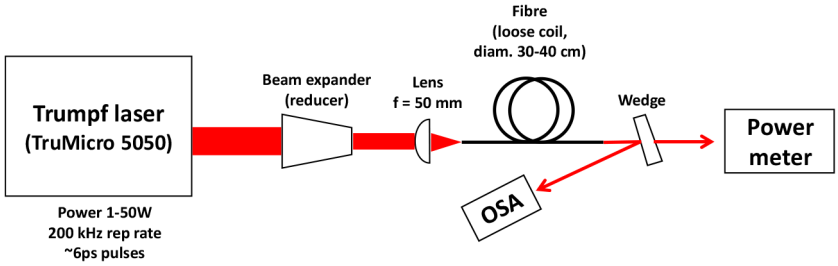

Fig. 2. Experimental setup including free space launching mechanism and measurement systems.

2.3 Experimental results

In this section, a range of experimental results for different pulse powers launched into a sample of each fiber will be presented and studied. To start with, we conducted our experiments with low power pulses, launched into 5m and 9.6m of atmospheric air-filled samples of HC-PBGF and HC-TF, respectively, to cover two different categories of HCFs and to study the effect of the fiber characteristics on the optical output. The measured output spectra for both fibers are shown in Fig. 3, for different average laser output power (P_{avg}). Coupling losses were ~0.3 dB and ~0.6 dB for the HC-TF and HC-PBGF respectively. In both cases, the measured output spectra show broadening around the pump wavelength caused by SPM, while sidebands start to appear at higher powers with consistent frequency detuning from the pump in both cases (as noted in Fig. 3(a,b)). The presented power levels in figures are measured at OSA and not representing the actual output power of the fibers.

Sidebands at 1036nm and 1023nm could in principle be caused by FWM, however, according to $2\gamma P_0 \approx -\beta_2\Omega^2 - (\beta_4/12)\Omega^4$ [40], the dependency of detuning on pulse power and dispersion should clearly affect the position of the peaks in both experiments, when dissimilar pulse powers and fibers are used. Here $\gamma, \beta_n, P_0, \Omega$ are the nonlinear coefficient, nth derivative of β, pump power, and phase matching detuning of Stokes respectively. To distinguish the FWM peaks from RRS peaks, in Fig. 3(c,d), we have plotted the phase matching condition (PMC) detuning for each P_{avg}. The phase matching condition for PBGF would be out of the range of the plotted spectrum. The clear difference between the phase

Optics EXPRESS

matching wavelengths and the actual peaks confirms the influence of RRS. In more detail, the first Stokes (1036 nm) and anti-Stokes Raman peaks (1023nm) appear at P_{avg} > 2W and P_{avg} > 5W for HC-TF and HC-PBGF, respectively. These frequency shifts are in a very good agreement with the rotational Raman shifts of Nitrogen (J = 6) and are consistent with the Nitrogen concentration in air (80%), while the different threshold powers at which the peaks begin to emerge can be explained by the difference in length and core size of each fiber. Meanwhile, the clear influence of nonlinear Kerr effects on the pulse and on the RRS peaks can be seen in the shape of the pump and sideband spectra [41]. Here, comparing two different categories of fibers has enabled us to understand the effect of fiber characteristics (primarily dispersion) on the emergence of broadening effects at their initial stages.

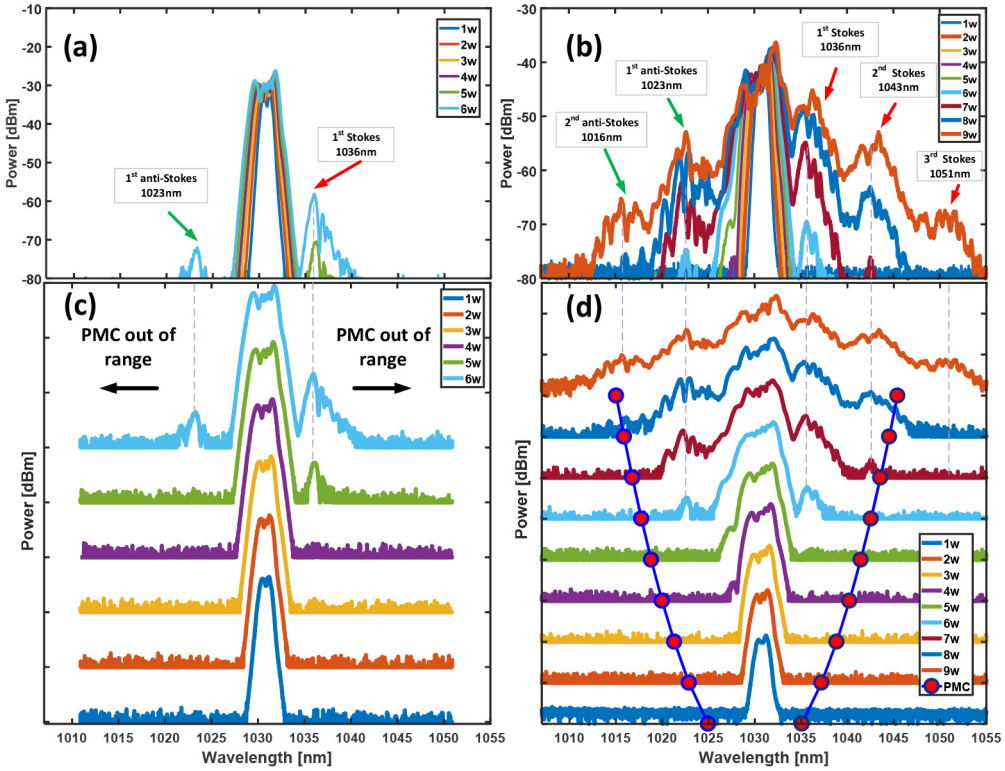

Fig. 3. The measured output spectrum of the pulsed laser with ~6 ps pulse length at 1030 nm launched in (a) 5 m of HC-PBGF with average laser power (Pavg) range of 1 - 6W and (b) 9.6 m of HC-TF with Pavg of 1 - 7W. The phase matching condition (PMC) detuning wavelengths are superposed over the experimental results for (c) HC-PBGF and (d) HC-TF with 10 dBm shift for each plot (10 dBm/div). The PMC is out of the plot range for HC-PBGF (d) due to the higher nonlinear coefficient of this fiber.

As the power increases (P_{avg} > 7W) for the HC-TF, higher orders of Stokes appear at is distinguishable in the output spectra. Although both fibers presented similar nonlinear outputs despite the markedly different dispersion properties, we found their damage thresholds to be considerably different. In the HC-TF, we could transmit up to 50W (P_{avg}), limited by the maximum power of our source, without observing any damage. In the HC-PBGF, however, we observed sudden damage to the end facet at a much lower input power level, resulting in the partial or complete destruction of the microstructure extending from the end-facet and several mm into the fibre. Repeated trials resulted in such damage occurring in a range of input power levels between 5 W and 9 W under similar coupling conditions. The

Optics EXPRESS

end-facet damage is attributed to power leakage into the clad-glass beyond the damage threshold of the glass.

Similar to the HC-TF, HC-KF has 2-3 order of magnitude lower power fraction in the glass than HC-PBGF and can tolerate higher power pulses. Therefore, to study nonlinear effects at higher powers we compared the HC-TF results with results obtained with a 13.8 m sample of our HC-KF (Fig. 1(c)). The wider transmission window with low loss profile in this latter fiber facilitates the study of VRS when the pulse power reaches the threshold for the first vibrational Stokes. Figure 4 (a,b) show the output spectrum of the HC-TF and HC-KF for P_{avg} = 10, 15, 20 W and P_{avg} = 2, 5, 10, 15, 20 W, respectively. As the power increases, the main pulse experiences broadening from a mixture of nonlinear phenomena initiated by RRS (e.g. higher order RRS, FWM, SPM, etc.) and long before any sign of VRS at P_{avg} = 20 W for HC-TF (Fig. 4(a)).

On the other hand, in the HC-KF, similar to the previous cases, sideband peaks with the same frequency shifts grow around similar input power (~5 W); this again confirms the insensitivity of the process to the fiber characteristics and the dominance of RRS. However, there is a clear sign of a 2330 cm^{-1} shifted peak (at ~1355 nm) associated with VRS of Nitrogen at P_{avg} = 5 W.

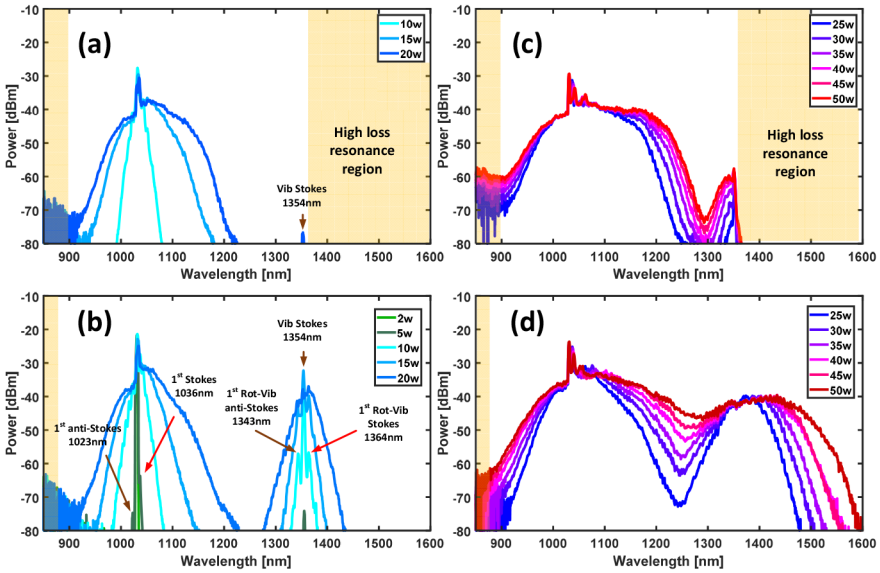

Fig. 4. The output spectrum of the pulsed laser with ~6ps length at 1030 nm launched in to (a) HC-TF with average laser power (P_{avg}) of 10, 15, 20 W and (b) HC-KF with P_{avg} of 2, 5, 10, 15, 20 W. The higher power output spectrums from overlapping sidebands to broad supercontinuum are presented for P_{avg} = 25, 30, 35, 40, 45 and 50W in (a) HC-TF and (b) HC-KF.

The difference of the VRS threshold in both cases mainly comes from the high loss of the HC-TF at the VRS wavelength (Fig. 1(f)) in comparison to that of the HC-KF, with minor effects arising from their characteristic differences (i.e. fiber length and core size). It can be seen how the pulse duration in this experiment results in a good balance between pump broadening and energy transfer to the vibrational levels, making it possible to distinguish the signature of VRS very clearly [20]. This effect is modeled in the following sections. Furthermore, the first sign of roto-vibrational Stokes and anti-Stokes scattering are clear around the main peak of VRS as labeled in Fig. 4(b) at P_{avg} = 10 W. This initiates the broadening effect of the VRS sidebands and which is similar to that at the main pump wavelength. At powers above ~20 W, the pump and vibrational Raman peaks experience a rapidly-growing broadening effect, which is initiated by the RRS lines of Nitrogen and is accelerated further by the Kerr nonlinearity with a similar pattern in both fibers, as seen in

Optics EXPRESS

Fig. 4(c,d). These broadening processes from pump and VRS peaks continue until they start overlapping and create a broadband supercontinuum extending over a bandwidth of ~750 nm in the HC-KF. In the case of the HC-TF, the high loss of the fiber outside the anti-resonance window reduces the bandwidth of the supercontinuum to only ~400 nm. On the other hand, the HC-KF output shows a very broad supercontinuum with a fairly flat feature (~10 dB over 500nm). In fact, such a broadband output is generated with the help of the spectral wings from the main pump and VRS peak (second pump) in the form of a 'dual pump' SG scheme. This, in principle, can decrease the required launched power to achieve a similar bandwidth in conventional 'single pump' broadening schemes for the same initial pulse width, since the necessary broadening in each 'pump' can be achieved with lower power.

The consistency in the position of the initial sideband peaks in all three fibers at low input power and the appearance of similar vibrational peaks followed by spectral broadening (in two of the fibers) confirms that the detailed nonlinearity of air has a more significant effect than the dispersion related to waveguiding effects due to the fibers. The possibility of observing the dynamics of the nonlinear process in this setup by only tuning the pump power ranging from control of the Stokes and anti-Stokes sidebands, large Raman frequency down conversion (VRS) to broadband SG, introduces a powerful and tunable source with high spectral power density and broadband spectral output for many applications. Moreover, the complex nonlinear evolution provides a good test and means of verifying our numerical model which is described in the next section.

3. Modelling high power pulse propagation in air-filled HC fiber

In order to model high-power pulse propagation in air-filled HCFs a robust method is needed to handle both the linear and nonlinear phenomena. Among many different methods and equations (e.g. coupled-mode Raman-FWM, Beam propagation method, etc.) [40], the Generalized nonlinear Schrödinger equation (GNLSE) is one of the most common, reliable and accurate equations to model the dynamics of pulse propagation in a nonlinear waveguide (i.e. optical fibers). The GNLSE can model a range of phenomena by including key elements from linear chromatic dispersion to delayed molecular nonlinear effects. Despite its success in many fields, the common models for air are not suited for this equation and the most recent studies on air-filled HCFs used a very simplified model for nonlinearity of air [19, 22, 42, 43], which struggles to correctly model the detailed nonlinear behavior of air. In this study we address this problem by adopting a more comprehensive model which we then validate through comparison with experimental results.

In general, it would be challenging to model the optical behavior of a gas mixture, due to the multi-molecule nature of the gas. However, in case of air, it can be significantly simplified by considering the diatomic model of Nitrogen (~80%) and Oxygen (~20%) as the dominant gases involved in the optical process. Although this can reduce the complexity of the process, including proper details in the model of each gas is crucial to produce realistic and reliable results, since oversimplification can generate discrepancies between simulations and experimental results.

Here, to present a comprehensive model for the nonlinear behavior of air in the adaptive form with the GNLSE and to also include propagation of the pulse throughout the air-filled fibers, the dynamics of the pulse is assumed to be governed by the GNLSE in a co-moving frame with the central frequency of the pulse. This formulation includes the loss, dispersion and nonlinear properties of air, as well as all the waveguiding properties of the fiber. It can be represented by:

$$\frac{\partial \bar{E}(z,\omega)}{\partial z} - iD(\omega)\bar{E}(z,\omega) = \cdots$$
$$i\sum_{j=1}^{2} K_j \gamma_j(\omega) F\left\{ E(z,t) \int_{-\infty}^{+\infty} R_j(T) \left| E(z,t-T) \right|^2 dT \right\}, \quad j = 1,2. \tag{2}$$

Optics EXPRESS

Here $\bar{E}(z,\omega)=F\{E(z,t)\}$ denotes the slowly varying envelope of the electromagnetic field in the frequency domain. $D(\omega)$ is the linear/dispersion operator of the GNLSE with the definition $D(\omega)=\beta(\omega)-\beta(\omega_0)-\beta_1(\omega_0)(\omega-\omega_0)+i\alpha(\omega)/2$, where $\beta(\omega)$ represents the frequency-dependent propagation constant of the fundamental mode in the air-filled fiber and $\beta_n(\omega_0)$ is the n[th] derivative of the propagation constant at the central frequency of the pulse (ω_0). $\alpha(\omega)$ is the loss operator, which contains the contribution of fiber loss and the Rayleigh absorption of air. *D(ω)*, consists of all higher order dispersion values in the frequency domain that are required to fully model the dispersion property of the material and the waveguide. The right hand side of the equation represents the nonlinearity originating from the interaction of the pulse with the multi-material waveguide, which here has two elements of air and glass represented by $j=1,2$, respectively. In order to model the relative contribution of glass and air in the nonlinear response, we have introduced K_j, which represents the power fraction in the j^{th} material (i.e. K_1 for air and K_2 for glass) and satisfies the condition $\sum K_j=1$. The frequency dependent nonlinear coefficient for each substance has been defined as $\gamma_j(\omega)=\omega\bar{n}_j(\omega)/cA_{eff}$ with $\bar{n}_j(\omega)$ as the nonlinear refractive index of the j^{th} substance and A_{eff} as the effective mode area.

The $R_j(t)$ represent the nonlinear response of the medium labeled by *j*, as each term of summation in Eq. (1) stands for the nonlinear effect of the related material. In this definition, the nonlinear response ($R_j(t)$) contains both the electronic response, with instantaneous action on the pulse (Kerr effect), and the slower molecular response (Raman response) [40]:

$$R_j(t)=(1-f_{r_j})\delta(t)+f_{r_j}H_j(t),\quad j=1,2.$$
$$\int_{-\infty}^{+\infty}R_j(t)dt=1. \tag{3}$$

Here, $H_j(t)$ is the Raman response of the molecules and f_{r_j} is the fractional contribution of the Raman response to the total nonlinear response. In the regime of moderately high pulse power (but still far from the ionization energy of the material), $H(t)$ is the most important function, that includes almost all nonlinear effects at the molecular level and that needs to be properly defined to achieve accurate results.

Considering the causality for the Raman response and using the Kramers-Kronig principle, the simplest form of nonlinear response can be defined in the well-established form of a single damped oscillator (SDO) [44], which is defined as $H(t)\propto u(t)e^{-t/\tau_d}\sin(t/\tau_o)$ where *u(t)* is the Heaviside function, τ_d is oscillator damping time, and τ_o is time constant controlling the oscillation period. This simple SDO with $\tau_d=32\,fs$, $\tau_o=12.5\,fs$ and $f_{r_2}=0.18$ can successfully model a variety of nonlinear effects in silica glass by reproducing its broad Raman gain. In extreme cases a more precise model is needed, as suggested in [15]. Extending this approach to the study of RRS in gases, can only provide an overall approximate response, which accounts for all RRS lines as one broad continuous response. This simplification replaces the effect of individual lines in favor of one simple overlaying envelope. In previous works on air-filled HCFs, the response of air in the GNLSE has been modeled mainly by considering Nitrogen as the dominant gas with $\tau_d=77\,fs$, $\tau_o=62.5\,fs$ and $f_{r1}=0.5$; this only takes into the account the 8th rotational transition in RRS of Nitrogen [14, 42]. To illustrate some disadvantages of the SDO model for air in our pulse length regime, a few experimental results of air-filled HC-KF (Fig. 4(b)) were simulated using the SDO and are shown in Fig. 5. Here, not only the SDO was unable to correctly model the initial position of the sideband peaks and broadening effects at low power, but it also

Optics EXPRESS

completely omits VRS, which is vital in this pulse duration regime, and therefore the SDO produces incorrect results. In the following, we describe the implementation of a comprehensive model of the air response using the GNLSE, which reproduces well the experimental results of different air-filled HCFs.

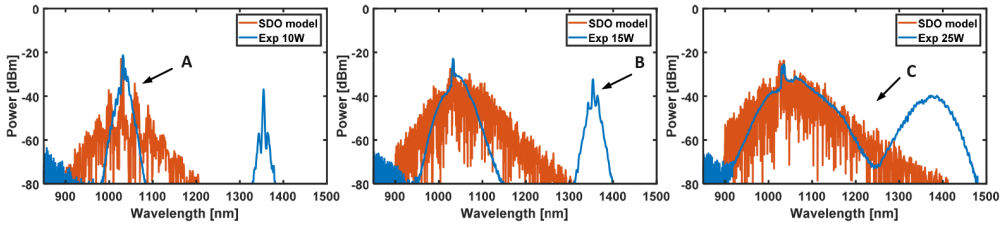

Fig. 5. Comparison between experimental results of air-filled HC-KF (Fig. 4(b)) and GNLSE simulation results using SDO model for air (a) P_{avg} = 10 W, (b) P_{avg} = 15 W, (c) P_{avg} = 25 W. The SDO model cannot properly predict A. the position of the RRS at low power. B. VRS is not reproduced at all. C. The broadening effect is not correctly reproduced due to lack of VRS.

3.1 Semi-quantum model for air

Unlike solid materials, where molecules are limited to vibrational states, it is well known that gases can also have rotational states, which can be involved in RRS (subject to their Raman activity). Although general modeling of rotational states and rotational scattering can be challenging for complex molecules, a semi-quantum model (SQM) for simple diatomic molecules, such as Nitrogen and Oxygen (most frequent molecules in air), can provide enough information and accuracy to model the behavior of the molecule in interaction with high power pulses. Generally, the full rotational Raman response of each gas is a collective response of transitions from individual rotational states, which depend on the energy level and population of each rotational state, as introduced in [45–47]. Although the quantum Schrödinger equation can be used to calculate the rotational states and their energy levels, thanks to a much less onerous classical approach to calculate the angular momentum and energy of rotational levels, the implementation of their quantum mechanical property is straightforward [48].

For linear diatomic molecules such as Nitrogen and Oxygen by considering a rigid linear rotor as their molecular model and implementing the angular momentum principle, the energy of an individual rotational state (J) can be calculated as $E_J = J(J+1)Bhc$, where B is the rotational constant of the rotor and h is Planck's constant. In this representation, RRS arises from rotational level changes caused by an excitation field. The excitation/ relaxation of rotational states creates rotational Raman Stokes/anti-Stokes, respectively, with a frequency shift proportional to the energy difference between the initial and final states of the molecule. However, the change in energy levels is not arbitrary, but determined by the selection rule of $\Delta J = \pm 2$ [48], which implies a rotational Raman frequency shift of $\omega_J = 2Bc(2J+3)$.

In addition to the frequency shift, the intensity of each individual transition is also needed to complete the model. For each Raman transition (ω_J), the intensity is proportional to the population of the initial state and the Placzek-Teller coefficient of transition from the initial to final state [49]. In more detail, the population of each state is defined by the Maxwell-Boltzmann thermal distribution, the quantum degeneracy of the initial state ($2J + 1$) and the isotopic effect. Taking all these factors into account, the total rotational Raman response of the diatomic gas ($H_{rot_k}(t)$) is ($k = 1, 2$ for N_2 and O_2) [13, 49, 50]:

Optics EXPRESS

$$H_{rot_k}(t) = u(t)C_{rot_k}\sum_J e^{(-t/\tau_{rot_{k,J}})}A_{k_J}\sin(4\pi B_k c(2J+3)),$$
$$A_{k_J} = (N_{k_{(J+2)}} - N_{k_J})q_{k_J}\frac{(J+2)(J+1)}{(2J+3)}, \quad (4)$$
$$N_{k_J} = \exp[-hcB_k J(J+1)/KT]. \quad k = 1,2.$$

where K, T are Boltzmann constant, and gas temperature, respectively. The rotational constants are $B_1 = 1.99\ cm^{-1}$ and $B_2 = 1.44\ cm^{-1}$. The quantum effects are $q_{1_J} = 1$ and 2 for odd and even J due to nuclear statistics (Isotopic effect), while $q_{2_J} = 1$ and 0 for odd and even J, respectively. In this approach, A_{K_J} represent the intensity of the Raman transition for frequency shift ω_J, which includes the effect of temperature by considering the temperature dependence of the population of molecules (N_{K_J}) for each rotational level. The normalization coefficient (C_{rot_k}) is defined to normalize the Raman response by Eq. (3). The relaxation factors ($\tau_{rot_{kJ}}$) are on average 61 ps and 68 ps for N_2 and O_2, respectively [48] while we used the measured values in [51]. Here, for the sake of simplicity, a few factors such as centrifugal force, Stark effect, etc. are not included in the model, which have a very small effect on the results in the experimental environment (i.e. temperature and pressure stability).

Figure 6(a) shows a comparison between the time domain rotational Raman response for Nitrogen using the SDO and Eq. (4) as SQM. Although the SDO can mimic the first oscillating part of the response (t < 1 ps) (inset of Fig. 6(a)), which may be enough to model the SG process initiated by high-power short pulses [19, 20], the lack of the other oscillating peaks affects the accuracy of the model in reproducing the mutual effects of the Raman and Kerr processes. This can be seen more clearly in the frequency domain, as shown in Fig. 6(b,c). The essential difference between the real and imaginary parts of both responses sets the major imbalance between the Raman and parametric gains in each model.

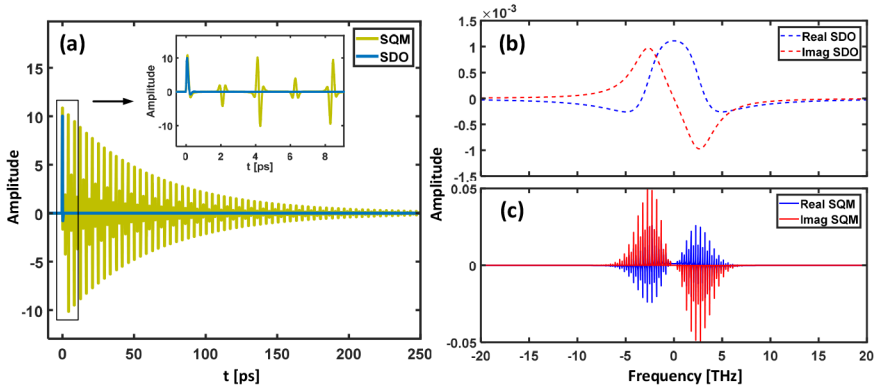

Fig. 6. (a) Comparison between the time domain rotational Raman response for Nitrogen by the SDO model and SQM, (c) real and imaginary parts of the frequency response of the SDO model for Nitrogen, (c) real and imaginary parts of the frequency response of SQM for Nitrogen.

Besides, the SDO model, not only cannot recreate the full rotational Raman response of the system, but it also fails to model the mutual interaction of rotational and vibrational states (roto-vibrational Raman scattering). Here, to achieve a full Raman response of the molecule we follow a similar approach as for the rotational states and include the roto-vibrational Raman transitions. The vibrational Raman response $H_{vib_k}(t)$ in the Q branches are:

Optics EXPRESS

$$H_{vib_k}(t) = u(t)C_{vib_k}\sum_J e^{(-t/\tau_{vib_{k_J}})}M_{k_J}\sin(\omega_{k_J}t),$$
$$\omega_{k_J} \approx 2\pi c\left(\bar{\Omega}_k - \eta_k J(J+1)\right), \quad (5)$$
$$M_{k_J} = q_{k_J}(2J+1)\exp\left[-hcB_k J(J+1)/KT\right], \quad k=1,2.$$

where $\bar{\Omega}_k$ is the central wavenumber of the roto-vibrational transition ($\bar{\Omega}_1 \approx 2330\ cm^{-1}$ and $\bar{\Omega}_2 \approx 1556\ cm^{-1}$) and η_k are the rotational and vibrational interaction constants ($\eta_1 \approx 0.0173\ cm^{-1}$ and $\eta_2 \approx 0.0159\ cm^{-1}$). C_{vib_k} is the normalization coefficient and the average value for τ_{vib_k} is considered to be 10 ps [52].

Finally, to complete the Raman response function of air, we combined the rotational and vibrational response of individual gases and took into account their concentration in air:

$$H_1(t) = \sum_{k=1}^{2}\frac{\sigma_k}{\bar{n}_1}\left[\mu_{rot_k}H_{rot_k}(t) + (1-\mu_{rot_k})H_{vib_k}(t)\right], \quad (6)$$

where $\bar{n}_1$ is the nonlinear refractive index of air. σ_k is the product of molecular concentration (80% for N_2 $(k=1)$ and 20% of O_2 $(k=2)$) and their nonlinear refractive index [13]. This represents the contribution of the individual gas molecules to the Raman response. μ_{rot_k} is the contribution of rotational response to the full response of the molecule, since the collective form of the response function should satisfy the normalization requirement (Eq. (3)) as much as the individual rotational and vibrational Raman response functions. Equation (6) contains all the necessary elements for a complete Raman model for air, from high order rotational transition for short frequency shifts to roto-vibrational phenomena for much higher frequency shifts, in a compatible form with use in a GNLSE.

3.2 Numerical modeling

To numerically model and reproduce the experimental results through the use of Eq. (2), a set of parameters are needed. To begin with, for each fiber the linear operator in Eq. (2) ($D(\omega)$) must be calculated from the experimental and simulated data in Fig. 1. In addition, the contribution of each individual effect must be tailored to the air nonlinearity through an experimental fitting process for (μ_{rot_k}, f_{r_k}).

Although the nonlinear part of Eq. (2) includes all the relevant effects, by assuming the frequency independence for $\bar{n}_j$ in the frequency range of experiment, one can significantly increase the numerical calculation speed by unifying separate convolutions in Eq. (2) into one as:

$$\frac{\partial\bar{E}(z,\omega)}{\partial z} - iD(\omega)\bar{E}(z,\omega) = i\gamma_{total}(\omega)F\left\{E(z,t)\int_{-\infty}^{+\infty}R_{total}(T)\left|E(z,t-T)\right|^2 dT\right\}. \quad (7)$$

Here $R_{total}(t) = (1-f_{r_{total}})\delta(t) + f_{r_{total}}H_{total}(t)$, $H_{total}(t) = 1/(\bar{n}_{total}f_{r_{total}})\sum_{j=1}^{N}K_j\bar{n}_j f_{r_j}H_j(t)$, $\bar{n}_{total} = \sum_{j=1}^{N}K_j\bar{n}_j$, $f_{r_{total}} = \sum_{j=1}^{N}K_j\bar{n}_j f_{r_j}/\bar{n}_{total}$, and $\gamma_{total} = \omega_0\bar{n}_{total}/cA_{eff}$.

By using this form of GNLSE, any number of materials can be included in the simulation without adding any extra computational burden. Also, despite its complex look, once Eqs. (4-6) are calculated using commonly accepted values in the literature for $\bar{n}_j$ at the experimental condition (i.e. T = 300 K, P = 1 atm) [13, 15] and at the initial time grid points of the

Optics EXPRESS

simulation, they can be included in the GNLSE without any extra computational cost, like one does with the SDO.

To model the pulse propagation dynamics, the modified GNLSE (Eq. (7)) was solved numerically by the split-step method with direct calculation of the linear part ($D(\omega)$), and by use of a fifth order Rung–Kutta method for the nonlinear operator [53], with an adaptive step approach [54] to increase efficiency and speed. Here, special care was taken to eliminate – through imposition of artificially high loss at long wavelengths – the spurious Raman peaks that might otherwise reappear at short wavelengths due to periodic boundaries of the FFT.

To fit the parameters of the model we used the experimental data of the HC-KF transmission experiment. Best fit was obtained for $\mu_{rot_1} = 0.986$, $f_{r_1} = 0.75$. We also imposed $\mu_{rot_2} = 1$ due to the absence of VRS for Oxygen in the experimental data. Figure 7 shows a comparison of experimental and simulation results for the HC-KF experiment, where we have reduced the sensitivity of the simulations to stochastic noise by averaging over 20 simulations for each spectrum.

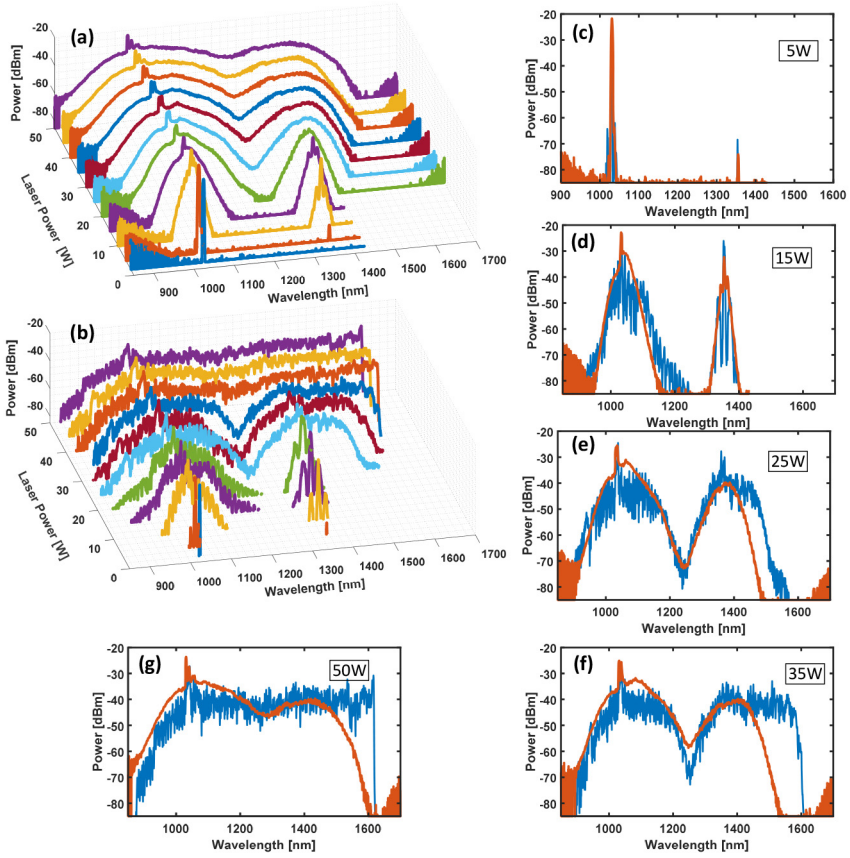

Fig. 7. (a) Experimental output spectra for HC-KF at different Pavg (Fig. 4(b.d)), (b) simulation results using SQM in the GNLSE for the HC-KF (averaged over 20 shots). The comparison of simulation and experimental results for (c) 5 W, (d) 15 W, (e) 25 W, (f) 35 W, (g) 50 W.

Excellent agreement can be seen at low input powers, where the simulations reproduce well both the RRS and VRS dynamics, Fig. 7(c). As the power increases the signature of higher order RRS, alongside the roto-vibrational Raman scattering is also well reproduced (Fig. 7(d)). As discussed previously, increasing the input power not only stimulates higher order Raman peaks, but it also produces noticeable broadenings from the Kerr nonlinearity,

Optics EXPRESS

which plays a key role in the sideband expansion. This broadening process is well reproduced, as shown by the snapshots at which the input laser and VRS bands start to overlap (Fig. 7(e,f), at ~1250nm). Such an accurate simulated behavior can only be possible thanks to the implementation of the full Raman response described above. As the input power increases further, the dynamics of the process become more sensitive to the parameters of the fiber. We believe that some of the discrepancies at the highest peak powers are mostly due to insufficiently inaccurate modeling of the dispersion in the vicinity of the VRS wavelength, which is close to the clad-core mode crossing of the fiber (~1360nm).

To further verify the model and the fitting values (μ_{rot_k} , f_{r_1}) mentioned above, we have also simulated the HC-TF. Selected comparisons between experimental and simulation results, showing again excellent agreement, are shown in Fig. 8. Key to obtaining such a good match was the careful reproduction of the loss profile of the fiber at VRS wavelengths. Such a good agreement of the model, with the same fitted parameters, for such different fibers, indicates the robustness of the modeling approach proposed here.

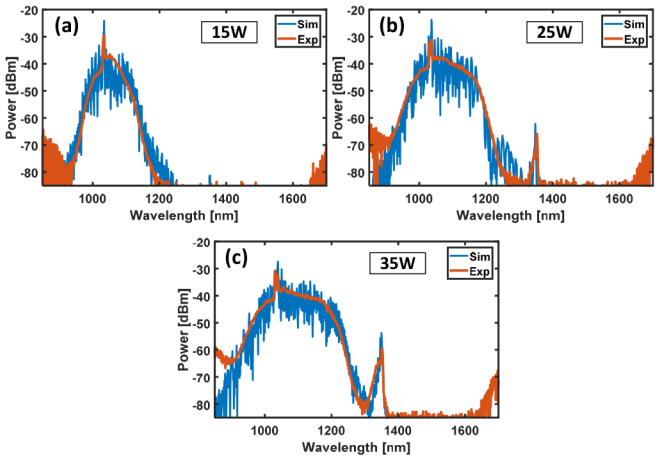

Fig. 8. Comparison of experimental output spectrum and simulation results using the SQM in the GNLSE for HC-KF for P_{avg} of (a) 15 W, (b) 25 W, (c) 35 W.

In these experiments, as previously discussed, the pulse duration plays a major role in the pulse evolution dynamics, and in particular on the observation or not of the VRS peak in the output spectrum. To demonstrate this point, we have used the previous model to study pulse propagation along the same 13.8m of HC-KF discussed above, for shorter (0.8 ps) and longer (50 ps) pulse durations. In both cases, we have conserved the pulse energy, 200 μJ, equivalent to the P_{avg} = 40 W for the 6 ps pulse above (i.e. 6 ps at 200 KHz repetition rate).

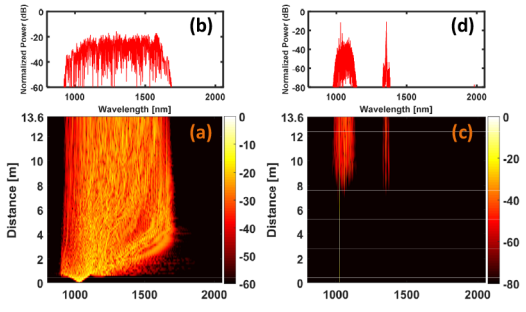

Fig. 9. Power spectrum evolution of a 800 fs pulse (a) propagating along HC-KF at 1030 nm with 200 μJ energy, (b) at the output of the fiber; (c) Power spectrum evolution of a 50 ps pulse propagating along HC-KF at 1030 nm with 200 μJ energy, (d) the power spectrum of the 50 ps pulse at the output of the fiber.

Optics EXPRESS

Figure 9(a) shows that for an 800 fs pulse, unlike the 6 ps pulse, the appearance of VRS features are masked by the faster broadening of the pulse due to soliton fission, soliton frequency shifting and other Kerr nonlinearities. The resulting output spectrum is a wide supercontinuum without any sign of VRS, which agrees with experimental observations [19, 20, 22]. In contrast, in the 50 ps case, Fig. 9(c,d), shows the clear appearance of a VRS peak, but the broadening of both the pump and the VRS bands are considerably less than in Fig. 7.

4. Conclusions and discussion

In this work, we have studied the nonlinear dynamics of nonlinear picosecond pulse evolution in state-of-the-art air-filled hollow core fibers. We have tested three different fiber types, HC-PBGF, HC-TF and HC-KF to explore the different behaviors and examine the influence of fiber characteristics on the results. In order to observe simultaneously Kerr and Raman effects and extensively model the nonlinear dynamics in air, we have selected input pulses of a few picosecond pulse duration; 6 ps pulses with a maximum energy of 250 μJ at 1030 nm from a commercial tabletop laser (TruMicro 5050©) were launched into the individual fibers. By comparing results for the HC-PBGF and HC-TF with very different fiber characteristics (i.e. dispersion and loss profile), we attributed the origin of certain sidebands to rotational Raman scattering in Nitrogen. By switching from HC-PBGF to HC-KF, necessary for the exploration of higher input powers, we observed the generation of a new band around VRS frequencies. At even higher powers, the bands around pump and VRS frequencies merged and we achieved a high spectral power density supercontinuum spanning from 850 to 1600 nm. The presented experimental setup is therefore not only a valuable platform to study the pulse propagation dynamics in air-filled HCFs, but potentially also a technologically relevant high power source with power-selectable tunable outputs, ranging from a highly efficient short/long range frequency conversion to broad supercontinuum generation.

To model the experimental results, we have shown that the well-established single damping oscillator (SDO) model is inadequate due to the lack of VRS and an oversimplified RRS interpretation. We have therefore adopted a semi-quantum model for air that not only includes the detailed RRS and VRS responses but that can also be used in conjunction with a standard GNLSE to simulate, very accurately, the broad dynamics of pulse propagation in the air-filled fiber. Using this model, we have simulated the experimental results for HC-KF and HC-TF with very good agreement, and studied the effect of pulse length on the nonlinear propagation dynamics. The model presented here can be used to precisely tailor the fiber design for either maximizing a specific nonlinear phenomenon, or to reduce the pulse distortion and energy dissipation caused by nonlinearity in pulse delivery applications. In future works, we intend to investigate the discrepancy between the model and experimental data for even higher peak power pulses and rotational Raman frequency shifts.

Funding

EPSRC Airguide Photonics (Grant number EP/P030181/1); the ERC Lightpipe project (grant agreement no. 682724); the Royal Society (NVW and DJR through the University Research Fellowship and Wolfson Research Merit Award schemes respectively).

Acknowledgments

The authors would like to thank Dr. Russell S Minns for constructive discussions regarding the air spectroscopy. Data published in this paper are available from the University of Southampton repository at http://doi.org/10.5258/SOTON/D0362.